

Crystallographic crack propagation rate in single-crystal nickel-base superalloys

Christian Busse^{1,*}, Frans Palmert^{2,3}, Paul Wawrzynek⁴, Björn Sjödin³, David Gustafsson³, and Daniel Leidermark¹

¹Division of Solid Mechanics, Linköping University, SE-58183 Linköping, Sweden

²Division of Engineering Materials, Linköping University, SE-58183 Linköping, Sweden

³Siemens Industrial Turbomachinery AB, SE-61283 Finspång, Sweden

⁴Fracture Analysis Consultants, Inc., Ithaca, New York, USA

Abstract. Single-crystal nickel-base superalloys are often used in the hot sections of gas turbines due to their good mechanical properties at high temperatures such as enhanced creep resistance. However, the anisotropic material properties of these materials bring many difficulties in terms of modelling and crack growth prediction. Cracks tend to switch cracking mode from Mode I cracking to crystallographic cracking. Crystallographic crack growth is often associated with a decrease in crack propagation life compared to Mode I cracking and this must be taken into account for reliable component lifing. In this paper a method to evaluate the crystallographic crack propagation rate related to a crystallographic crack driving force parameter is presented. The crystallographic crack growth rate is determined by an evaluation of heat tints on the fracture surface of a specimen subjected to fatigue loading. The complicated crack geometry including two crystallographic crack fronts is modelled in a three dimensional finite element context. The crack driving force parameter is determined by calculating anisotropic stress intensity factors along the two crystallographic crack fronts by finite-element simulations and post-processing the data in a fracture mechanics tool that resolves the stress intensity factors on the crystallographic slip planes in the slip directions. The evaluated crack propagation rate shows a good correlation for both considered crystallographic cracks fronts.

1 Introduction

There is always a strive towards higher combustion temperatures when designing industrial gas turbines used for power generation, due to the resulting increase in efficiency and reduction in terms of pollution [1]. These ever increasing temperatures put high requirements on many components in the hot sections of the gas turbines. One crucial component that is exposed to this harsh environment is the blade in the first turbine stage. These blades are therefore often manufactured from nickel-base superalloys cast as single-crystals, due to their great material properties under these conditions. Nevertheless, the complex nature of the anisotropy of these materials is often a challenge in terms of testing, modelling and understanding the fracture behaviour [2-8]. Cracks have been observed to change cracking mode from Mode I to cracking on crystallographic slip planes [9-10], cf. Fig.1. Since single-crystal nickel-base superalloys contain an inherent internal structure of distinct crystallographic slip planes and slip directions, it is physically motivated to assume that these crystallographic planes are potential critical planes for crack initiation and crack growth [10]. Crystallographic cracking differs from Mode I cracking in its mechanisms, resulting in a different resistance

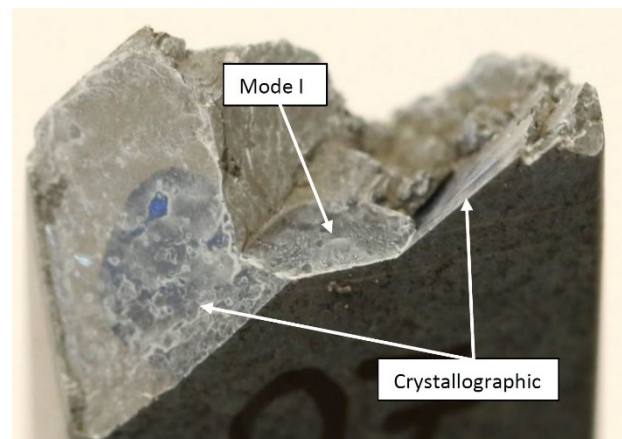


Fig. 1: Fracture view of the specimen Kb1 with visible crystallographic and Mode I cracking

towards crack growth. The Mode I crack growth behaviour is well understood and easier to model compared to the crystallographic cracking mode, where this knowledge is lacking. One major aspect complicating the modelling of the behaviour of single-crystal materials is the misalignments from the nominal crystal orientation influencing the stress state and thus the fracture behaviour [11]. Especially three-dimensional

* Corresponding author: christian.busse@liu.se

crack growth modelling, incorporating crystallographic cracking, has not been attempted due to its complexity. The aim of this paper is to evaluate and model the crack growth rate for crystallographic cracking. This has been done by evaluating a Resolved Stress Intensity Factor (RSIF) on the crystallographic crack fronts and correlating it to a crack growth law. The parameters in the crack growth law have been calibrated by evaluating heat-tinted fracture surfaces of performed experiments.

2 Material and experiments

The investigated material is a single-crystal nickel-base superalloy of face-centred cubic structure (FCC), similar to the alloy described by Reed *et al.*[12]. Its main alloying elements, in order of decreasing wt %, are as follows: Ni-Cr-Ta-Co-Al-W-Mo-Si-Hf-C-Ce.

As the specimen is cast as a single grain they possess anisotropic properties, where the elastic stiffness constants for 500 °C are presented in Table 1. The temperature of 500 °C has been chosen since it corresponds to the temperature during normal operation at the blade fir tree root, which is a critical location in the blade design.

Table 1. Elastic stiffness constants, units in GPa.

| Temp. [°C] | C_{11} | C_{12} | C_{44} |
|------------|----------|----------|----------|
| 500 | 201.9 | 127.0 | 112.8 |

To study the crack growth behaviour and its effects on the studied single-crystal nickel-base superalloy material, an isothermal fatigue crack growth experiment at 500 °C was performed. Isothermal conditions were chosen due to their simpler nature compared to thermo-mechanical fatigue conditions. The test specimen geometry was a surface flawed fatigue crack growth specimen of Kb-type [13], henceforth denoted as Kb specimen. The geometry of the Kb specimen can be seen in Fig. 2. The specimen was manufactured from a cast bar with the casting direction parallel to the nominal [001] crystallographic direction. The secondary orientation [010] was normal to the wide surface on which the flaw was introduced. The surface flaw, of semi-elliptical shape, was introduced by electro

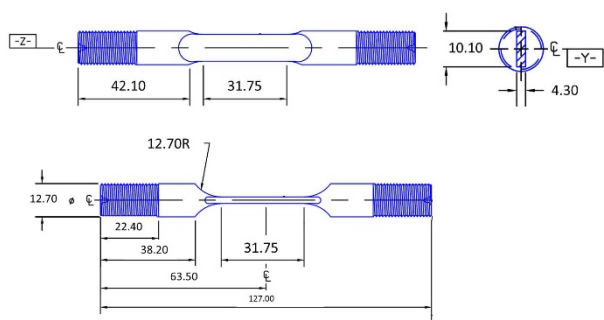


Fig. 2: Kb specimen geometry. Units in mm.

discharge machining to a depth of 0.127 mm

and width of 0.245 mm centred on the gauge section of the specimens. The misalignments from the nominal crystallographic orientations in terms of sequential rotations about the nominal [010], [100] and [001] directions are 1.7°, 0.1° and -2.8°, respectively. The misalignments are determined by measuring the visible dendrites on three polished and etched orthogonal surfaces on the specimen. For a detailed description see [14].

The fatigue crack growth testing of the Kb specimen was done according to the guidelines provided in the ASTM E647 [15] test specification. The test was run in an MTS servo-hydraulic testing machine with a test capacity of 89 kN. The specimen was precracked at room temperature, with a frequency of 10 Hz to initiate a crack. After this, the fatigue crack growth test was performed according to the test conditions shown in Table 1. Three heat tints were created in each test by maintaining an open crack and increasing the temperature to 704°C under a hold time of eight hours. The crack length was monitored using direct current potential drop measurement (DCPD) according to [16].

Table 2. Test conditions.

| Temperature [°C] | Stress ratio R_σ [-] | Frequency [Hz] |
|------------------|-----------------------------|----------------|
| 500 | 0.05 | 0.5 |
| Max. Force [N] | Nominal loading Direction | |
| 19857 | [001] | |

2.1 Fracture surfaces

After the experiments were finished, the fracture surfaces were examined, and as can be seen in Fig. 1, the cracking mode transitions from Mode I into crystallographic cracking on each side. Further examination in a Scanning Electron Microscope (SEM) at the instances where the two cracking modes intersect was performed. An example is depicted in Fig. 3, where the cracking modes transition on the right side of the Mode I crack is shown. It can also be observed that the progressing crystallographic crack front advanced on a crystallographic slip plane beneath the Mode I crack front. The higher magnification on the right image suggests that the crystallographic crack grew beneath the Mode I crack all the way from the free surface.

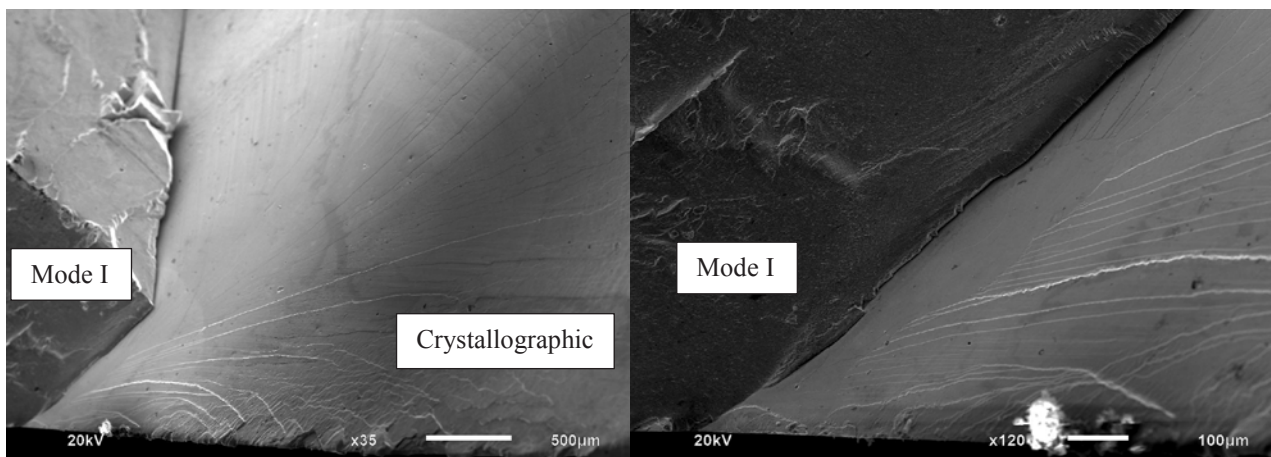


Fig. 3: SEM image of the transition of cracking modes, showing (left) the crystallographic crack front advancing beneath the Mode I crack front and (right) the mutual crack front at the surface.

Furthermore, the fracture surfaces have been studied in an optical microscope in order to evaluate the crack front shapes for the different heat tints. The heat tints are shown for the visible parts of the crystallographic and the Mode I crack in Fig. 4, where they are highlighted in blue, green and red. It is to be pointed out that only the last two heat tints provide information about the crack front shapes of the crystallographic cracks fronts. The crack shapes of the hidden portions of the two crystallographic crack fronts (on the left and on the right side of the Mode I crack front) have been approximated and are represented by the dashed contours in Fig. 4. In the following, the crack instances outlined by the green and red contours and associated to the second and third heat tints are referred to as crack instance 1 and 2, respectively. From the analysed fracture surfaces it can be concluded that each crack instance includes three intersection crack fronts, *i.e.* two crystallographic fronts and one Mode I front.

Each heat tint is associated to a number of loading cycles until that specific crack shape is formed. The heat tints

associated with the number of cycles are presented in Table 3, where N_0 , N_1 and N_2 represent the number of cycles until crack instance 0, 1 and 2 is reached. Crack instance 0 is disregarded in the following since no crystallographic cracking is associated to it. Furthermore, the fracture surfaces were scanned in an Atos Triple Scan machine to acquire a 3D representation of the fracture surfaces in terms of mesh data. This data, in conjunction with the optical images is used to create a realistic mapping of the crack shape into a mesh representation. This procedure is elaborated in Section 4.1.

Table 3. Experimental results of the number of cycles for the different heat tints.

| Heat tints | N_0 | N_1 | N_2 |
|------------|--------|--------|--------|
| Cycles | 203678 | 217426 | 218827 |

The 3D representations of the fracture surfaces have also been used to determine the crystallographic cracking

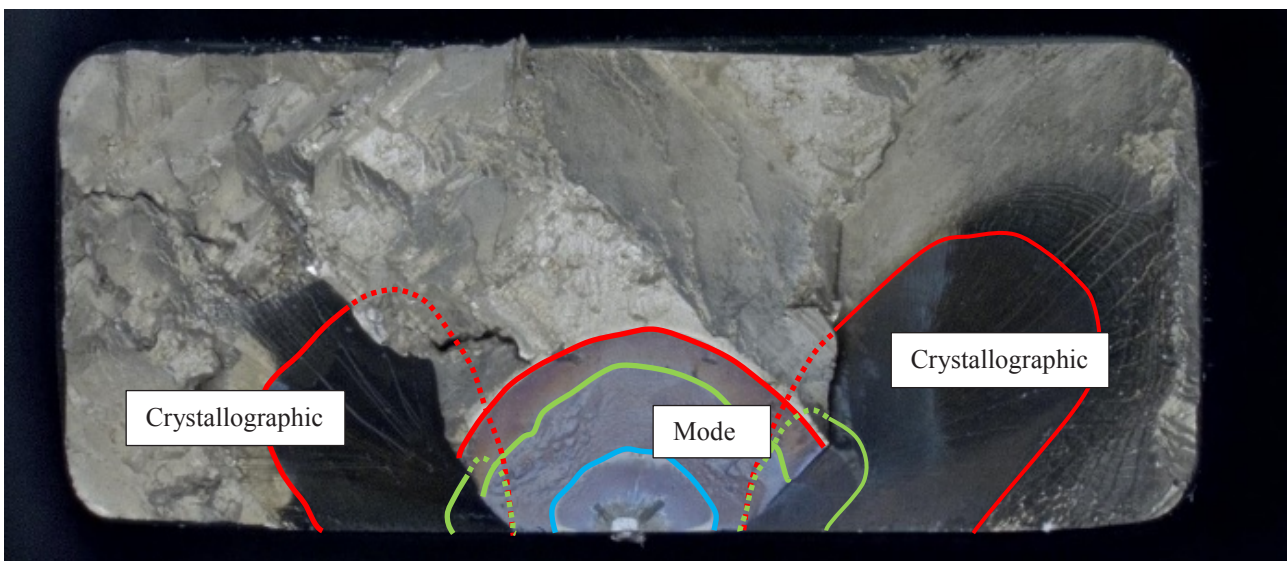


Fig. 4: Heat tints on fracture surface of specimen Kb1. Cracks instances 0, 1 and 2 are highlighted in blue, green and red, respectively.

planes by determining its normal vector. The active crystallographic cracking planes are $\bar{1}\bar{1}\bar{1}$ and $\bar{1}\bar{1}\bar{1}$ in terms of Miller notation for the left and right side of the Mode I crack front, respectively.

3 Crystallographic crack driving force and crack growth rate

In order to evaluate the crystallographic crack growth rate an appropriate crack driving force parameter has to be adopted. A RSIF k_{EQ} for the crystallographic portions of the crack was used. This parameter is employed in a crack growth model as proposed by Paris *et al.* [17] as:

$$\frac{dL}{dN} = C_c (k_{EQ})^{n_c}, \quad (1)$$

where Eq. (1) represents the crack growth model for crystallographic cracking with the parameters C_c and n_c , and dL/dN is the crystallographic crack growth rate. The entity L is defined as the orthogonal distance between the crystallographic crack fronts of the two crack instances, see the dotted line Fig. 5, where the discretized crack fronts are schematically illustrated. Based on the performed experiments, only the shape of the crystallographic fronts of the crack instances 1 and 2 are known. Under the assumption, that crack growth occurs orthogonal to the crack front, the orthogonal distance between two points along the crack fronts of the two crack instances corresponds to $L(i)$, where i describes the positions along the crack front. For each position i , two k_{EQ} values and associated number of cycles are determined. These relations are then used to calibrate the parameters C_c and n_c by fitting the crack growth data in a log-log diagram of the crack growth rate over the crack driving force parameter. This is schematically shown in Fig. 6, where the subscript of N and the superscript of k_{EQ} indicate the crack instance number. From two corresponding $k_{EQ}(i)$ values the mean value was used for the crack propagation rate evaluations below. The difference in loading cycles

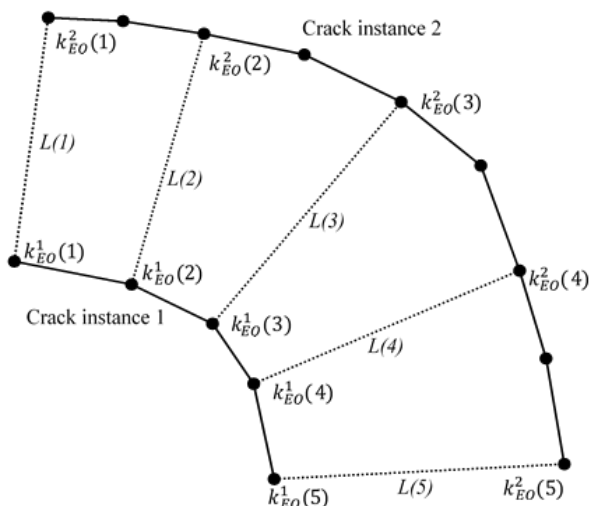


Fig. 5: Representation of the nodes pairs of crack instance 1 and 2 and corresponding RSIF and L.

ΔN_{2-1} between crack instance 2 and 1 is constant for all points along the crack fronts and has the value 1401 cycles. Thus, the following approximation is used: $dL/dN \approx L/\Delta N_{2-1}$, where $k_{EQ} = (k_{EQ}^1 + K_{EQ}^2)/2$. When considering the discretised crack front in Fig. 5, it can be seen that the crack fronts of both crack instances can have a different number of nodes. Thus not all nodes on both crack fronts are accounted for.

The correct choice of crack driving force parameter is vital for a meaningful prediction of the crack growth rate. The equivalent RSIF k_{EQ} used in this work describes the singular stress field resolved onto the crystallographic slip planes in the Burgers' directions. This is due to the fact that the deformations in these materials are localised to the crystallographic slip planes in the Burgers' directions, and are associated with the dislocation motion [18]. As there are three Burgers' directions per crystallographic slip plane, the direction resulting in the highest k_{EQ} is chosen for each point along the crack fronts in the crack growth model evaluation shown below. Thus, the RSIF parameter k_{EQ} is evaluated for each point along the two crack fronts in the three Burgers' directions on the corresponding crystallographic slip planes.

The equivalent RSIF k_{EQ} is based on anisotropic Stress Intensity Factors (SIFs) (K_I , K_{II} and K_{III}), which can be evaluated in different ways. The approach in this work has been by using the Displacement Correlation Method (DCM) with incorporation of anisotropic material properties and accounting for the material misalignments. The DCM matches crack opening displacements computed using the finite element method with theoretical expressions for the near crack-front displacement fields developed by Hoenig [19] as follows:

$$u_i = \frac{\sqrt{2r}}{\pi} Re(\sum_{j=1}^3 m_{ij} N_{jl}^{-1} K_l Q_j), \quad (2)$$

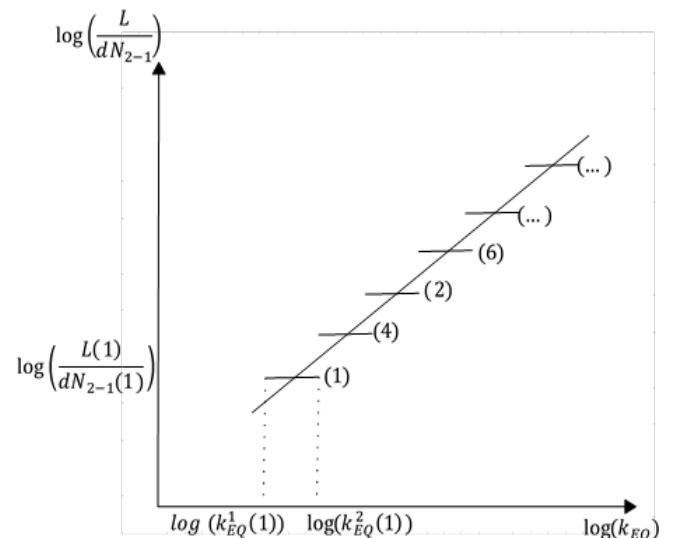


Fig. 6: Schematic example of the crystallographic crack growth rate over the RSIF in a log-log diagram

$$\begin{pmatrix} u_1 - u_1' \\ u_2 - u_2' \\ u_3 - u_3' \end{pmatrix} = -\sqrt{\frac{8l}{\pi}} \begin{bmatrix} \text{Re}(m_{1j}N_{j1}^{-1}\sqrt{p_j}) & \text{Re}(m_{1j}N_{j2}^{-1}\sqrt{p_j}) & \text{Re}(m_{1j}N_{j3}^{-1}\sqrt{p_j}) \\ \text{Re}(m_{2j}N_{j1}^{-1}\sqrt{p_j}) & \text{Re}(m_{2j}N_{j2}^{-1}\sqrt{p_j}) & \text{Re}(m_{2j}N_{j3}^{-1}\sqrt{p_j}) \\ \text{Re}(m_{3j}N_{j1}^{-1}\sqrt{p_j}) & \text{Re}(m_{3j}N_{j2}^{-1}\sqrt{p_j}) & \text{Re}(m_{3j}N_{j3}^{-1}\sqrt{p_j}) \end{bmatrix} \begin{Bmatrix} K_I \\ K_{II} \\ K_{III} \end{Bmatrix}, \quad (3)$$

where Re represents the real part of the quantities in parenthesis, two repeated indices obey the summation convention from 1 to 3, the directions 1, 2 and 3, and coordinates r and θ refer to the crack-front coordinate system illustrated in Fig 7., and K_j are the anisotropic SIFs K_I , K_{II} , and K_{III} . It is assumed that the stresses and displacements are functions only of the in-plane coordinates r and θ . The quantities, m_{ij} , N_{ij} , and Q_i are defined in [20]. Consider the near crack-front configuration shown in Fig. 8, with two points A and A', which are on opposing crack faces a distance l from the crack front. Substituting $Q_j = \sqrt{\cos \theta + p_j \sin \theta}$, $\theta = \pi$,

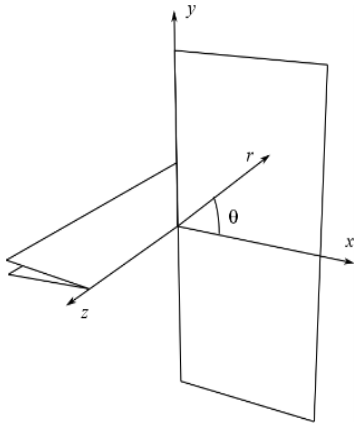


Fig. 7: Crack front Cartesian and cylindrical coordinate system.

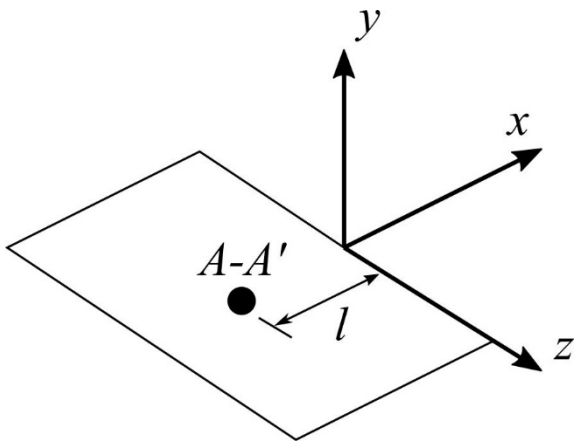


Fig. 8: Local coordinate system and configuration used to compute stress intensity factors with DCM.

and $r = l$ into Eq. (2) results in Eq. (3), which can then be solved for the stress intensity factors with a summation over $j = 1, 2, 3$.

Based on the anisotropic SIFs, the stress field around the crack tip is calculated using the descriptions of the stresses near the crack tip in an anisotropic material developed by Hoenig [19]. The use of a 3D-analysis

enables the evaluation the RSIFs for every point along the crack fronts allowing for stress evaluations throughout the thickness of the model. The local stress tensor is given by:

$$\sigma' = \frac{1}{\sqrt{2\pi r}} \mathbf{f}'(K_I, K_{II}, K_{III}, \theta), \quad (4)$$

where the entities r and θ are the distance from the crack front and the angle from which the crack front is approached. The superscript denotes that the stress tensor is scaled to account for Burgers' direction from which the crack front is approached, which does not necessarily lie in the plane orthogonal to the crack front. Further information and the definition of the tensor \mathbf{f}' is given in the submitted manuscript by Busse *et al.* [14].

The stress tensor in Eq. (4) is then projected on the crystallographic slip planes with the normal \mathbf{n} in the directions \mathbf{n} , \mathbf{s} and \mathbf{t} and multiplied by $\sqrt{2\pi r}$, yielding the definitions of the RSIFs in the three modes of fracture on a crystallographic plane:

$$k_I = \mathbf{n} \cdot \mathbf{f}'(K_I, K_{II}, K_{III}, \gamma, \beta) \cdot \mathbf{n}, \quad (5)$$

$$k_{II} = \mathbf{s} \cdot \mathbf{f}'(K_I, K_{II}, K_{III}, \gamma, \beta) \cdot \mathbf{n}, \quad (6)$$

$$k_{III} = \mathbf{t} \cdot \mathbf{f}'(K_I, K_{II}, K_{III}, \gamma, \beta) \cdot \mathbf{n}, \quad (7)$$

This is illustrated in Fig. 9. As all modes of fracture are assumed to influence the crack growth behaviour, an equivalent crystallographic crack driving force parameter is defined by:

$$k_{EQ} = \sqrt{\psi k_I^2 + k_{II}^2 + k_{III}^2}, \quad (8)$$

The Mode I RSIF is scaled with ψ , which is a calibration parameter based on experiments in order predict correct

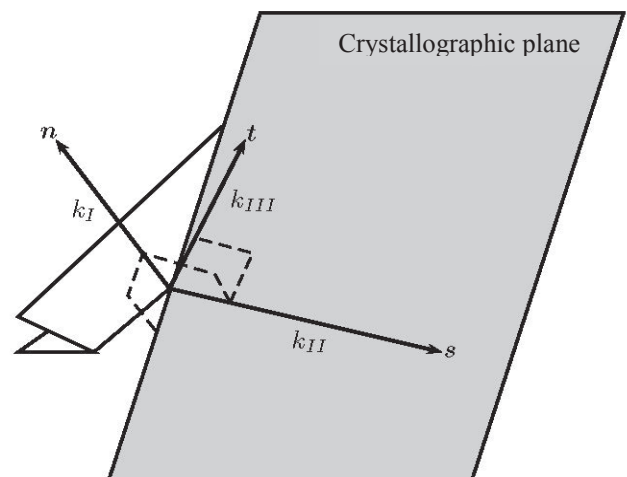


Fig. 9: Illustration of the directions of the RSIFs.

crystallographic cracking planes along a Mode I crack front. Further details can be found in [14].

4 Simulations and evaluations

In order to determine the crystallographic crack driving forces for both crack instances an FE-model of the Kb specimen has been built. The following boundary conditions were applied; a fixed support at one of the circular surfaces and a concentrated force to one master node on the other circular surface. This force corresponds to the one in the experiment. The master node was coupled to all other nodes of the surface by a constraint that restrained motion in the plane and gave an equal deformation in the axial direction. The equivalent RSIF was then calculated along the crack fronts where crystallographic cracking is present and the conventional anisotropic SIFs are calculated for the parts of Mode I cracking. This is done for the cracks corresponding to the heat tints, since the crack geometry can be approximated best. The anisotropic SIFs are calculated by the crack evaluation tool FRANC3D [21]. The FE-solver of ABAQUS [22] is used to calculate the displacements. It should be pointed out that no singular elements were used at the crack fronts. This may lead to a less accurate capturing of the \sqrt{r} singularity and thus affecting the quality of the calculated SIF values.

4.1 Fracture surfaces

In order to represent the experiments in meaningful manner the crack geometries corresponding to the above described heat tints are modelled. For this, the outlined crack front contours, *cf.* Fig. 4, are projected from the 2D top view on the 3D representation of the scanned fracture surface. The created 3D crack geometry corresponding to the heat tints of crack instance 1 and 2 are then transformed into a FE-mesh for the further analysis. The 3D mesh consisting of triangle shell elements was then converted into a volumetric void with a distance of 0.1 mm between the crack flanks allowing the computation of the SIFs for the complex crack geometry with three intersecting crack fronts. The corresponding 3D mesh for crack instance 1 is shown in Fig. 10, where the three different sections of the crack can be seen. On each crack geometry three different crack fronts are defined, corresponding to both crystallographic and the Mode I crack fronts as explained above.

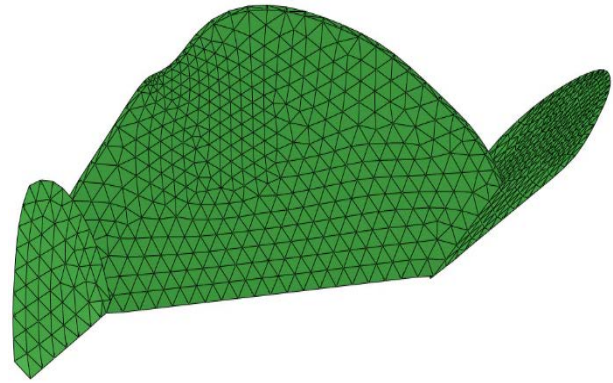


Fig. 10: 3D FE-mesh representation of the geometry of crack instance 1.

5 Results and Discussion

The equivalent RSIFs for the crystallographic crack fronts for the two considered crack instances are evaluated along the parts of the crack fronts, which are visible in the optical microscope. Furthermore, the nodes close to the free surface were disregarded due to the inaccuracies in the determination of the anisotropic SIFs. This is mainly due to poorly shaped elements causing local errors and a different order of the singularity. Even though not all points along the crack fronts were used to evaluate the crystallographic crack growth rate, it was important to model the whole geometry of the crack to capture the state more accurately.

The calibration parameter ψ necessary to predict the correct crystallographic cracking plane after a transition from Mode I cracking, as described in [14], was initially set to a value of 0.1 based on experimental results. In the referenced study, the RSIF was calculated along a Mode I crack and not along crystallographic crack fronts as in the current study. In this work, the RSIFs along the crystallographic crack front were evaluated using different ψ values, where the best correlation to the considered crack growth law was achieved by a ψ value of zero, meaning that once the crack grows on a crystallographic plane, the resolved shear stresses are the main driving forces. The resulting Resolved Shear Stress Intensity Factor (RSSIF) is then

$$k_{RSS} = \sqrt{k_{II}^2 + k_{III}^2}. \quad (9)$$

The evaluated entities are then plotted in log-log diagram of the crystallographic crack growth rate of the crack driving force as described above. The results are shown Fig. 11, where it can be seen that all data points for both crystallographic cracks fall into a narrow band. The blue squares correspond to the left and the orange squares to the right crystallographic crack front. A power fitting was used to determine the parameters C_c and n_c to the values of $C_c = 3.155 \cdot 10^{-4}$ mm/cycle and $n_c = 0.6594$. The corresponding fitting curve is also shown in

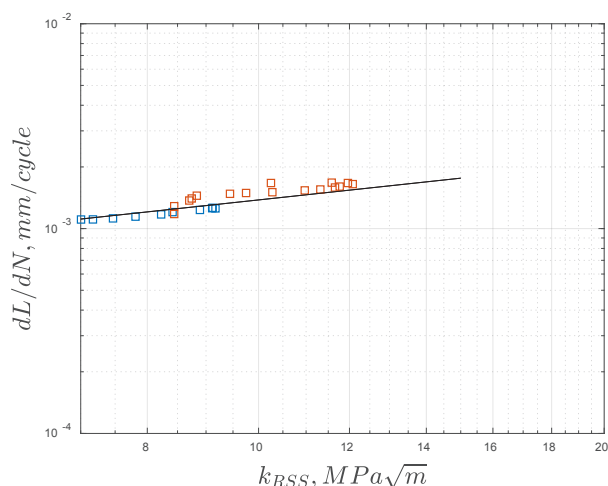


Fig. 11: Crystallographic crack propagation rate

5.1 Uncertainties and future work

It should be noted that the actual crack geometries for the crack instances 1 and 2 are only partly known and, as described above, the sections hidden beneath the Mode I portion of the crack are approximated. Thus, the stress state along the crack fronts in the experiment deviates from the one in the simulation. The error depends on the quality of the approximation. Furthermore, uncertainties in the determination of the misalignments can alter the stress state and thus influence the modelling of crack driving forces. As described above, the quality of the evaluated SIFs should be verified as future work by a comparison to a different method for calculating SIFs. Work to compute SIFs by a conservative crack front integral is ongoing. Furthermore, comparisons to different experiments are needed to verify the determined parameters.

6 Conclusions

- The data points of the crystallographic crack propagation rate collapse on a small band for both crystallographic cracks indicating a correlation between crystallographic crack propagation rate and the determined crystallographic crack driving force.
- A comparison to different experiments is needed to verify the determined parameters.
- 3D crack growth modelling of complex crack geometries with multiple intersecting crack

fronts could be achieved, but the quality of the determined SIFs needs to be verified

Acknowledgments

This research has been funded by the Swedish Energy Agency and Siemens Industrial Turbomachinery AB through the Research Consortium of Materials Technology for Thermal Energy Processes, Grant no. KME-702, the support of which is gratefully acknowledged.

References

- [1] A. Pineau and S. D. Antolovich, "High temperature fatigue of nickel-base superalloys - A review with special emphasis on deformation modes and oxidation," *Eng. Fail. Anal.*, vol. **16**, no. 8, pp. 2668–2697, (2009).
- [2] D. Leidermark, J. J. Moverare, K. Simonsson, S. Sjöström, and S. Johansson, "Room temperature yield behaviour of a single-crystal nickel-base superalloy with tension/compression asymmetry," *Comput. Mater. Sci.*, vol. **47**, no. 2, pp. 366–372, (2009).
- [3] D. P. Pope and S. S. Ezz, "Mechanical properties of Ni3Al and nickel-base alloys with high volume fraction of gamma prime," *Int. Met. Rev.*, vol. **29**, no. 3, pp. 136–167, (1984).
- [4] M. Segersäll, J. J. Moverare, D. Leidermark, and K. Simonsson, *Low-cycle fatigue behaviour of a Ni-based single-crystal superalloy*, vol. **891–892**. (2014).
- [5] D. Leidermark and M. Segersäll, "Modelling of thermomechanical fatigue stress relaxation in a single-crystal nickel-base superalloy," *Comput. Mater. Sci.*, vol. **90**, pp. 61–70, (2014).
- [6] R. L. Amaro, S. D. Antolovich, R. W. Neu, and A. Staroselsky, "Physics-Based Modeling of Thermo-Mechanical Fatigue in PWA 1484," in *Superalloys 2012*, (2012), pp. 481–490.
- [7] B. F. Antolovich, A. Saxena, and S. D. Antolovich, "Fatigue crack propagation in single-crystal CMSX- 2 at elevated temperature," *J. Mater. Eng. Perform.*, vol. **2**, no. 4, pp. 489–495, (1993).
- [8] J. Telesman and L. J. Ghosn, "The unusual near-threshold FCG behavior of a single crystal superalloy and the resolved shear stress as the crack driving force," *Eng. Fract. Mech.*, vol. **34**, no. 5–6, pp. 1183–1196, (1989).
- [9] J. Telesman and L. J. Ghosn, "Fatigue crack growth behavior of PWA 1484 single crystal superalloy at elevated temperatures," *J. Eng. Gas Turbines Power*, vol. **118**, no. 2, pp. 399–405, (1996).
- [10] D. Leidermark, J. Moverare, K. Simonsson, and S. Sjöström, "A combined critical plane and

- critical distance approach for predicting fatigue crack initiation in notched single-crystal superalloy components,” *Int. J. Fatigue*, vol. **33**, no. 10, pp. 1351–1359, (2011).
- [11] C. Busse *et al.*, “A finite element study of the effect of crystal orientation and misalignment on the crack driving force in a single-crystal superalloy,” in *Proceedings of the ASME Turbo Expo*, (2016), vol. **7A–2016**.
- [12] R. C. Reed, J. Moverare, A. Sato, F. Karlsson, and M. Hasselqvist, “A New Single Crystal Superalloy for Power Generation Applications,” *Superalloys 2012*, pp. 197–204, (2012).
- [13] A. Coles, R. E. Johnson, and H. G. Popp, “Utility of surface-flawed tensile bars in cyclic life studies,” *J. Eng. Mater. Technol. Trans. ASME*, vol. **98**, no. 4, pp. 305–315, (1976).
- [14] C. Busse *et al.*, “Prediction of crystallographic cracking planes in single-crystal nickel-base superalloys,” *Manuscr. Submitt. Publ.*, (2018).
- [15] ASTM, “Test Method for Measurement of Fatigue Crack Growth Rates,” (2012).
- [16] K. Schwalbe and D. Hellmann, “Application of the Electrical Potential Method to Crack Length Measurements using Johnson’s Formula,” *J. Test. Eval.*, vol. **9**, no. 3, pp. 218–221, (1981).
- [17] P. C. Paris and F. Erdogan, “A Critical Analysis of Crack Propagation Laws,” *Journal of Basic Engineering*, vol. **85**, no. 4, p. 528, 1963.
- [18] D. R. Askeland and P. P. Phule, *The Science and Engineering of Materials*, Fifth Edit. Toronto: Thomson, Canada, (2006).
- [19] A. Hoenig, “Near-tip behavior of a crack in a plane anisotropic elastic body,” *Eng. Fract. Mech.*, vol. **16**, no. 3, pp. 393–403, (1982).
- [20] L. Banks-Sills, P. A. Wawrzynek, B. Carter, A. R. Ingraffea, and I. Hershkovitz, “Methods for calculating stress intensity factors in anisotropic materials: Part II-Arbitrary geometry,” *Eng. Fract. Mech.*, vol. **74**, no. 8, pp. 1293–1307, (2007).
- [21] FRANC3D, *FRANC3D Reference Manual*. Ithaca, USA: Fracture Analysis Consultants Inc., (2016).
- [22] ABAQUS, *ABAQUS 6.12 Documentation*. Providence, USA: Dassault Systèmes, (2014).